

Hundreds of weak lensing shear-selected clusters from the Hyper Suprime-Cam Subaru Strategic Program S19A data

Masamune OGURI^{1,2,3}, Satoshi MIYAZAKI^{4,5}, Xiangchong LI^{2,3}, Wentao LUO³, Ikuyuki MITSUISHI⁶, Hironao MIYATAKE^{7,6,3}, Surhud MORE^{8,3}, Atsushi J. NISHIZAWA⁷, Nobuhiro OKABE^{9,10,11}, Naomi OTA¹², Andrés A. PLAZAS MALAGÓN¹³ and Yousuke UTSUMI¹⁴

¹Research Center for the Early Universe, University of Tokyo, Tokyo, 113-0033, Japan

²Department of Physics, University of Tokyo, Tokyo 113-0033, Japan

³Kavli Institute for the Physics and Mathematics of the Universe (Kavli IPMU, WPI), University of Tokyo, Chiba 277-8582, Japan

⁴National Astronomical Observatory of Japan, 2-21-1 Osawa, Mitaka, Tokyo 181-8588, Japan

⁵SOKENDAI (The Graduate University for Advanced Studies), Mitaka, Tokyo, 181-8588, Japan

⁶Division of Physics and Astrophysical Science, Graduate School of Science, Nagoya University, Nagoya 464-8602, Japan

⁷Institute for Advanced Research, Nagoya University, Nagoya 464-8601, Japan

⁸The Inter-University Center for Astronomy and Astrophysics (IUCAA), Post Bag 4, Ganeshkhind, Pune 411007, India

⁹Department of Physical Science, Hiroshima University, 1-3-1 Kagamiyama, Higashi-Hiroshima, Hiroshima 739-8526, Japan

¹⁰Hiroshima Astrophysical Science Center, Hiroshima University, 1-3-1 Kagamiyama, Higashi-Hiroshima, Hiroshima 739-8526, Japan

¹¹Core Research for Energetic Universe, Hiroshima University, 1-3-1 Kagamiyama, Higashi-Hiroshima, Hiroshima 739-8526, Japan

¹²Department of Physics, Nara Women's University, Kitauoyanishi-machi, Nara, Nara 630-8506, Japan

¹³Department of Astrophysical Sciences, Princeton University, Peyton Hall, Princeton, NJ 08544, USA

¹⁴Kavli Institute for Particle Astrophysics and Cosmology, SLAC National Accelerator Laboratory, Stanford University, Menlo Park, CA 94025, USA

*E-mail: masamune.oguri@ipmu.jp

Received (reception date); Accepted (acceptation date)

Abstract

We use the Hyper Suprime-Cam Subaru Strategic Program S19A shape catalog to construct weak lensing shear-selected cluster samples. From aperture mass maps covering $\sim 510 \text{ deg}^2$ created using a truncated Gaussian filter, we construct a catalog of 187 shear-selected clusters that correspond to mass map peaks with the signal-to-noise ratio larger than 4.7. Most of the shear-selected clusters have counterparts in optically-selected clusters, from which we estimate the purity of the catalog to be higher than 95%. The sample can be expanded to

418 shear-selected clusters with the same signal-to-noise ratio cut by optimizing the shape of the filter function and by combining weak lensing mass maps created with several different background galaxy selections. We argue that dilution and obscuration effects of cluster member galaxies can be mitigated by using background source galaxy samples and adopting the filter function with its inner boundary larger than about $2'$. The large samples of shear-selected clusters that are selected without relying on any baryonic tracer are useful for detailed studies of cluster astrophysics and cosmology.

Key words: dark matter — galaxies: clusters: general — gravitational lensing: weak — large-scale structure of universe

1 Introduction

Clusters of galaxies are the most massive gravitationally bound objects in the Universe and have proven to be a key class of objects for establishing the standard cosmological model that consists of dark matter and dark energy (see e.g., Allen et al. 2011; Kravtsov & Borgani 2012, for reviews). We can study the internal structure and statistical property of clusters of galaxies with multi-wavelength datasets, including optical, X-ray, and radio. For instance, a massive cluster of galaxies can be securely identified from an overdensity of cluster member galaxies with similar colors (e.g., Gladders & Yee 2000). X-ray from hot gas in clusters of galaxies provides an important means of finding and studying clusters of galaxies (e.g., Ebeling et al. 2001). Large samples of clusters are being constructed via the Sunyaev-Zel'dovich effect on cosmic microwave background fluctuations (e.g., Planck Collaboration et al. 2016; Hilton et al. 2021).

The abundance and internal structure of clusters of galaxies are mainly determined by the dynamics of dark matter, which makes it critically important to study the distribution of dark matter in clusters in great detail. Weak gravitational lensing directly probes the dark matter distribution in clusters of galaxies and hence plays a key role in characterizing clusters (see e.g., Umetsu 2020, for a review). Among others, weak gravitational lensing plays an essential role for the use of the cluster population as a probe of cosmological parameters, because cluster observables must be linked to cluster masses in order to compare the observed abundance of clusters with theoretical predictions (see e.g., Pratt et al. 2019, for a review). Indeed, attempts to use clusters as an accurate cosmological probe have often been hampered by the uncertainty of mass calibrations of clusters for which complicated selection biases in cluster surveys must be taken into account.

A new approach that has been explored less extensively is finding clusters directly from weak gravitational lensing shear data by identifying peaks in weak lensing mass maps

(e.g., Schneider 1996; White et al. 2002; Hamana et al. 2004; Hennawi & Spergel 2005; Maturi et al. 2005, 2010; Fan et al. 2010; Marian et al. 2012; Lin et al. 2016). The abundance of the peaks contains information on the abundance of massive dark matter halos and hence on cosmological parameters (e.g., Jain & Van Waerbeke 2000; Dietrich & Hartlap 2010; Maturi et al. 2010; Shan et al. 2014; Liu et al. 2015a, 2015b; Hamana et al. 2015; Kacprzak et al. 2016; Shan et al. 2018). In addition, the relatively simple and clean selection function of weak lensing shear-selected clusters (e.g., Hamana et al. 2012; Chen et al. 2020) enables to use them for better understanding of cluster astrophysics. For instance, the X-ray analysis of shear-selected clusters suggests that they tend to be X-ray underluminous compared with clusters found in other techniques (Giles et al. 2015; Miyazaki et al. 2018a).

However a challenge lies in the requirement of wide and deep imaging for finding a significant number of weak lensing shear-selected clusters. First attempts identified only a handful of such clusters, if restricted to those with a sufficiently high signal-to-noise ratio (see e.g., Appendix 1) of $\gtrsim 5$ (Wittman et al. 2001; Miyazaki et al. 2002; Hettterscheidt et al. 2005; Wittman et al. 2006; Miyazaki et al. 2007; Schirmer et al. 2007; Gavazzi & Soucaill 2007; Utsumi et al. 2014). On the other hand, more systematic search of weak lensing shear-selected clusters is made possible thanks to recent progress of wide-field imaging surveys. For instance, Shan et al. (2012) constructed a sample of 51 shear-selected clusters with signal-to-noise ratios larger than 4.5 from the Canada-France-Hawaii Telescope Legacy Survey (Heymans et al. 2012).

Hyper Suprime-Cam (HSC; Miyazaki et al. 2018b), which is a wide-field optical imager mounted on the Subaru 8.2-meter telescope, offers a unique opportunity for constructing a large sample of weak lensing shear-selected clusters (Miyazaki et al. 2015). In particular, the HSC Subaru Strategic Program (HSC-SSP; Aihara et al. 2018b, 2018a, 2019), which is a deep multi-band imaging survey of 1400 deg^2 of the sky, is an ideal survey for this purpose.

Miyazaki et al. (2018a) presented a sample of 65 weak lensing shear-selected clusters with signal-to-noise ratios larger than 4.7 from the HSC-SSP first year shape catalog covering $\sim 160 \text{ deg}^2$ (Mandelbaum et al. 2018a). Using the same HSC S16A data, Hamana et al. (2020) constructed a sample of 124 shear-selected clusters with signal-to-noise ratios larger than 5 by mitigating the dilution effect of foreground and cluster member galaxies.

In this paper, we present updated catalogs of weak lensing shear-selected clusters from the latest HSC-SSP S19A shape catalog covering $\sim 433 \text{ deg}^2$ (Li et al., in prep.). We construct catalogs using three different approaches adopting different shapes of filters. We also assign redshifts of individual clusters by cross matching the shear-selected clusters with optically-selected clusters.

This paper is organized as follows. The data used for our analysis are summarized in section 2. Our method to construct mass maps is detailed in section 3. We present our main results in section 4, and conclude in section 5. Throughout the paper we assume the matter density $\Omega_m = 0.3$, the cosmological constant $\Omega_\Lambda = 0.7$, the baryon density $\Omega_b = 0.05$, the dimensionless Hubble constant $h = 0.7$, the spectral index $n_s = 0.96$, and the normalization of the matter power spectrum $\sigma_8 = 0.81$.

2 Data

2.1 Weak lensing shape catalog

The HSC-SSP S19A shape catalog (Li et al., in prep.) is constructed in a manner similar to the HSC-SSP S16A shape catalog presented in Mandelbaum et al. (2018a) that takes a moment-based approach of Hirata & Seljak (2003). The multiplicative and additive biases are derived with realistic image simulations (Mandelbaum et al. 2018b). The detailed systematics tests presented in Li et al., in prep. indicate that the S19A shape catalog is sufficiently accurate and is ready for various cosmological and astrophysical analyses. The catalog contains ~ 36 million galaxies.

Photometric redshifts of individual galaxies are also measured with various methods using the HSC *grizy*-band photometry (see Tanaka et al. 2018, for photometric redshifts of galaxies in the S16A data). In this paper we may use subsamples of the S19A shape catalog that are defined based on these photometric redshifts. Specifically, we define subsamples using the so-called P-cut method (see Oguri 2014; Medezinski et al. 2018), for which galaxies satisfying

$$\int_{z_{\min}}^{z_{\max}} P(z) dz > P_{\text{th}}, \quad (1)$$

where $P(z)$ the probability distribution function (PDF)

of the photometric redshift of each galaxy, are included. This P-cut allows us to securely and flexibly select galaxies behind clusters of interest by choosing the parameters z_{\min} , z_{\max} , and P_{th} appropriately (see Medezinski et al. 2018), and hence mitigate the dilution effect by cluster member galaxies (see also Hamana et al. 2020). The performance of the P-cut method is shown to be comparable to the selection of background galaxies in color-color space (Medezinski et al. 2018).

Throughout the paper we adopt the **dNNz** photometric redshift measurement (Nishizawa et al., in prep.) for defining background galaxy samples with the P-cut method. The **dNNz** is based on the multiple-layer perceptron that consists of six hidden layers where each layer contains 100 nodes. Input attributes are **cmodel** magnitude, size, and point spread function matched aperture magnitude in five broad bands, leading to 15 attributes in total, for each galaxy. The outputs are probabilities of the galaxy lying at the redshift bin spanning from $z=0$ to 7 divided into 100 bins. The code is trained to minimize the total difference between the output probabilities and input delta-function like probability summed over all training sample and redshift ranges. From the analysis on the test sample that has not been used for training, it is found that redshifts are accurate at the bias of 10^{-4} , the scatter of 3%, and the outlier fraction of less than 10%. The **dNNz** can avoid the overfitting even when the part of the data is missing (e.g., due to the lack of images in some broadband filters), by introducing a dropout layer right after the input layer with missing rate being 0.2. When applying the **dNNz** on the real data, the **dNNz** with the dropout layer is applied only when the part of the data is missing, otherwise the **dNNz** without the dropout layer is employed for the complete data to maximize the performance of the photometric redshift measurement.

2.2 Optically-selected cluster catalogs

We use several optically-selected cluster catalogs to assign redshifts for individual peaks in weak lensing mass maps. First, we adopt a cluster catalog (S20A version 1¹) constructed with the photometric data from the HSC-SSP S20A internal data release using the CAMIRA algorithm (Oguri 2014). In Oguri et al. (2018a), the CAMIRA algorithm has been applied to the HSC-SSP S16A data covering $\sim 230 \text{ deg}^2$ to construct a catalog of 1921 clusters

¹ While the S20A version 2 CAMIRA cluster catalog for which photometry corrections to mitigate various photometry issues (Aihara et al. 2019) are included is currently available, in this paper we use the version 1 catalog that was the latest version when the shear-selected cluster catalogs were constructed.

at redshift $0.1 < z < 1.1$ and richness N greater than 15 (see Oguri 2014, for the definition of richness N in the CAMIRA algorithm). In this paper, we adopt an updated catalog of 8910 clusters at redshift $0.1 < z < 1.38$ and richness greater than 15 from the HSC-SSP S20A data covering $\sim 830 \text{ deg}^2$.

Since the HSC-SSP survey region is chosen to overlap with the Sloan Digital Sky Survey (SDSS; York et al. 2000), we also use cluster catalogs from the SDSS for assigning cluster redshifts. Specifically, we use the redMaPPer cluster catalog (Rykoff et al. 2014) that contains clusters at $0.08 < z < 0.6$ as well as the WHL15 cluster catalog (Wen et al. 2012; Wen & Han 2015) that contains clusters at $0.05 < z < 0.79$. Both of these cluster catalogs were constructed based on the photometric galaxy catalog covering $\sim 14,000 \text{ deg}^2$ from SDSS Data Release 8 (DR8; Aihara et al. 2011). In addition to these purely optically-selected clusters, we also adopt the CODEX cluster catalog (Finoguenov et al. 2020) that contains clusters at $0.05 < z < 0.69$ from ROSAT all-sky survey (RASS; Voges et al. 1999) with optical confirmations using the redMaPPer algorithm applied to the SDSS DR8 data. Throughout the paper we use X-ray centroids as centers of the CODEX clusters.

All the cluster redshifts we adopt throughout this paper are photometric redshifts of clusters derived from the HSC *grizy*-band photometry for CAMIRA or from the SDSS *ugriz*-band photometry for redMaPPer, WHL15, and CODEX. The typical accuracy of these cluster photometric redshifts is $\sigma_z/(1+z) \sim 0.01$, which is sufficiently accurate for our current purpose.

3 Mass maps

3.1 Introduction

Since both convergence κ and shear γ are derived by the second derivatives of the lens potential, we can derive a convergence (mass) map from the shear map by a convolution of the shear map with a kernel (Kaiser & Squires 1993). More generally, in the flat sky coordinate θ , we can construct a map of the aperture mass $M_{\text{ap}}(\theta)$ (Schneider 1996), which is a convergence convolved with a spatial filter U

$$M_{\text{ap}}(\theta) = \int d\theta' \kappa(\theta') U(|\theta - \theta'|). \quad (2)$$

Provided that the spatial filter is compensated

$$\int d\theta \theta U(\theta) = 0, \quad (3)$$

it is equivalent to the convolution of the tangential shear with a kernel Q

$$M_{\text{ap}}(\theta) = \int d\theta' \gamma_+(\theta'; \theta) Q(|\theta - \theta'|), \quad (4)$$

where $\gamma_+(\theta'; \theta)$ is the tangential shear at θ' defined with respect to θ and Q is related with U as

$$Q(\theta) = \frac{2}{\theta^2} \int_0^\theta d\theta' \theta' U(\theta') - U(\theta). \quad (5)$$

In this paper, we consider two types of the spatial filters. One is a truncated Gaussian filter, which resembles the one adopted in Miyazaki et al. (2018a) to construct a shear-selected cluster sample from the HSC S16A data (see also Hamana et al. 2020). The other is a filter introduced by Schneider (1996), which we call a truncated isothermal filter throughout the paper and is designed to optimize the detection of halos from mass maps. In the next subsections, we describe these filters in more detail.

3.2 Truncated Gaussian filter

We use the following kernel function to define the truncated Gaussian filter

$$Q(\theta) = \frac{1}{\pi \theta^2} \left[1 - \left(1 + \frac{\theta^2}{\theta_0^2} \right) e^{-\theta^2/\theta_0^2} \right] e^{-\theta^4/\theta_{\text{out}}^4}, \quad (6)$$

which is smoothly truncated at $\theta = \theta_{\text{out}}$. Thus the filter is slightly different from the one adopted in Miyazaki et al. (2018a) and Hamana et al. (2020) for which the kernel function is sharply truncated at $\theta = \theta_{\text{out}}$. We adopt this smoothly truncated form for the numerical stability of our approach to derive mass maps using the Fast Fourier Transform (see subsection 3.4). The corresponding spatial filter $U(\theta)$ can be derived as

$$U(\theta) = -Q(\theta) - \int_0^\theta d\theta' \frac{2}{\theta'} Q(\theta'). \quad (7)$$

Throughout the paper we adopt $\theta_0 = 1.5'$ and $\theta_{\text{out}} = 13'$ so that resulting signal-to-noise ratios roughly matches those in Miyazaki et al. (2018a) and in Chen et al. (2020). Following Miyazaki et al. (2018a), we also do not apply any cut in the source galaxy sample. Hereafter this set-up is referred to as TG15.

3.3 Truncated isothermal filter

Schneider (1996) introduced the following form of the spatial filter for the aperture mass

$$U(\theta) = \begin{cases} 1 & (\theta \leq \nu_1 \theta_R) \\ \frac{1}{1-c} \left(\frac{\nu_1 \theta_R}{\sqrt{(\theta - \nu_1 \theta_R)^2 + (\nu_1 \theta_R)^2}} - c \right) & (\nu_1 \theta_R \leq \theta \leq \nu_2 \theta_R) \\ \frac{b}{\theta_R^3} (\theta_R - \theta)^2 (\theta - \alpha \theta_R) & (\nu_2 \theta_R \leq \theta \leq \theta_R) \\ 0 & (\theta_R \leq \theta) \end{cases} \quad (8)$$

where c , b , α are determined from the condition that $U(\theta)$

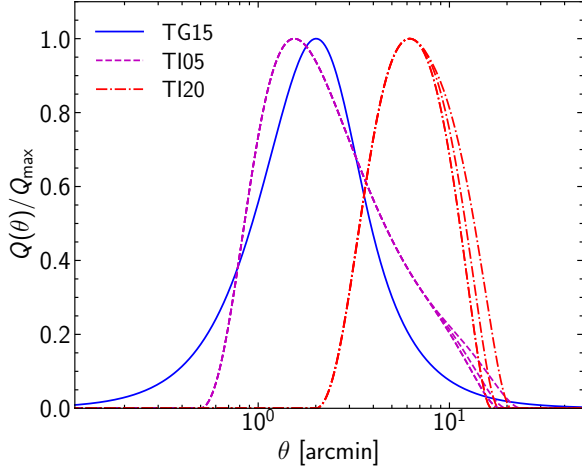


Fig. 1. The kernel function $Q(\theta)$, which is used to derive the aperture mass map (see equation 4), is shown. Solid, dashed, and dash-dotted lines are $Q(\theta)$ for the TG15, TI05, and TI20 set-ups summarized in Table 1. Note that we adopt slightly different shapes of $Q(\theta)$ for different source galaxy selections. We show $Q(\theta)$ normalized by its maximum value.

and its first derivative are continuous at $\theta = \nu_2 \theta_R$ as well as the compensation condition given by equation (3). This means that the shape of $U(\theta)$ is specified by three parameters, ν_1 , ν_2 , and θ_R . The corresponding kernel function is derived using equation (5).

This filter has several desirable properties. First, we can tweak the shape of the filter quite flexibly by adjusting the three parameters ν_1 , ν_2 , and θ_R . Second, it has $Q(\theta) = 0$ at $\theta < \nu_1 \theta_R$ and hence allows us to efficiently remove the contribution from the innermost part of halos, which is a source of various systematic effects such as the dilution effect by cluster member galaxies, the effect of reduced shear, and the magnification bias, to the signal. Third, the filter is confined within a finite radius (i.e., $U(\theta) = Q(\theta) = 0$ at $\theta > \theta_R$) and hence mitigate the impact of e.g., the boundary of the survey region to the map.

To explore the impact of the different inner boundary of the filter, $\nu_1 \theta_R$, in this paper we consider two different values of the inner boundary, $\nu_1 \theta_R = 0'.5$, and $2'$, which are referred as TI05 and TI20, respectively. For both TI05 and TI20, we construct mass maps with four different source galaxy subsamples defined using photometric redshifts of source galaxies (see subsection 2.1), in order to enhance the detection efficiency particularly at high redshifts (see also Hamana et al. 2020). For each inner boundary of the filter and the source galaxy sample, we carefully choose parameter values of the filter to maximize the expected signal-to-noise ratio and to mitigate the impact of density fluctuations along the line-of-sight on cluster finding. The specific procedure of the optimization of the parameters is detailed in Appendix 1. Table 1 summarizes set-ups to

construct shear-selected cluster samples. The shapes of the kernel function $Q(\theta)$ used in this paper are also presented in Figure 1.

3.4 Practical procedure

Following Oguri et al. (2018b), we adopt the Fast Fourier Transform (FFT) to derive aperture mass maps from the shape catalog. For a given source galaxy sample, we first create a shear map in a two-dimensional rectangular grid by a simple tangent plane projection. Throughout the paper, a pixel scale of the grid (θ -coordinate) of $\Delta\theta = 0'.25$ is adopted. We use a discrete version of equation (4) with weights to derive an aperture mass map i.e.,

$$M_{\text{ap}}(\theta_i) = \frac{(\Delta\theta)^2}{W(\theta_i)} \sum_j w_j \{\gamma_+(\theta_j; \theta_i) - c_{+,j}\} Q(|\theta_i - \theta_j|), \quad (9)$$

$$W(\theta_i) = \frac{\sum_j w_j (1 + m_j) Q(|\theta_i - \theta_j|)}{\sum_j Q(|\theta_i - \theta_j|)}, \quad (10)$$

where i and j label each grid, w_i is the weight of i -th grid that is computed from the sum of weights of sources galaxies in the grid, and $c_{+,i}$ and m_i denote the additive and multiplicative biases in the i -th grid, respectively. We evaluate these summations by FFT with an appropriate zero padding beyond the boundary. We also note that, due to the tangent plane projection, the principal axes of the θ -coordinate are not necessarily aligned with the North and West directions, even for the HSC-SSP S19A patches (see below) whose areas are relatively small. Since the shear in the HSC-SSP shape catalog is defined with respect to the equatorial coordinate system, we rotate the shear so that the shear is converted to the one defined with respect to the θ -coordinate. Furthermore, since the operation to create an aperture mass map (equation 9) is confined within a relatively small sky area thanks to the compact size of the convolution kernel $Q(\theta)$, the flat-sky approximation is expected to be locally accurate in deriving each pixel value of the aperture mass map.

Since the HSC-SSP S19A shape catalog consists of six disjoint patches (XMM, VVDS, WIDE12H, GAMA09H, GAMA15H, and HECTOMAP), we create mass maps for each of these patches to search for peaks.

We define signal-to-noise ratios of peaks using local estimates of the shape noise from the “sigma map” (Oguri et al. 2018b). We derive the sigma map by randomly rotating the orientations of source galaxies before constructing the mass map, and repeating this procedure 500 times. The sigma map is given by the square root of the variance of the randomized mass maps. The signal-to-noise ratio ν is defined by the ratio of the peak value of the mass map to the noise value at the peak position from the sigma

Table 1. Summary of set-ups to construct shear-selected cluster samples.

Name	Filter	Parameter values	Source galaxy selection	Num. of galaxies
TG15	Truncated Gaussian	$\theta_0 = 1'.5, \theta_{\text{out}} = 13'$	No cut	35804886
TI05	Truncated isothermal	$\nu_1 = 0.021, \nu_2 = 0.36, \theta_R = 23'.8$	$z_{\text{min}} = 0.2, z_{\text{max}} = 7, P_{\text{th}} = 0.95$	32750421
	Truncated isothermal	$\nu_1 = 0.025, \nu_2 = 0.36, \theta_R = 20'.0$	$z_{\text{min}} = 0.3, z_{\text{max}} = 7, P_{\text{th}} = 0.95$	26024748
	Truncated isothermal	$\nu_1 = 0.027, \nu_2 = 0.36, \theta_R = 18'.5$	$z_{\text{min}} = 0.5, z_{\text{max}} = 7, P_{\text{th}} = 0.95$	20664165
	Truncated isothermal	$\nu_1 = 0.027, \nu_2 = 0.36, \theta_R = 18'.5$	$z_{\text{min}} = 0.7, z_{\text{max}} = 7, P_{\text{th}} = 0.95$	15564223
TI20	Truncated isothermal	$\nu_1 = 0.095, \nu_2 = 0.36, \theta_R = 21'.1$	$z_{\text{min}} = 0.2, z_{\text{max}} = 7, P_{\text{th}} = 0.95$	32750421
	Truncated isothermal	$\nu_1 = 0.110, \nu_2 = 0.36, \theta_R = 18'.2$	$z_{\text{min}} = 0.3, z_{\text{max}} = 7, P_{\text{th}} = 0.95$	26024748
	Truncated isothermal	$\nu_1 = 0.121, \nu_2 = 0.36, \theta_R = 16'.6$	$z_{\text{min}} = 0.5, z_{\text{max}} = 7, P_{\text{th}} = 0.95$	20664165
	Truncated isothermal	$\nu_1 = 0.121, \nu_2 = 0.36, \theta_R = 16'.6$	$z_{\text{min}} = 0.7, z_{\text{max}} = 7, P_{\text{th}} = 0.95$	15564223

map. We note that the sigma map derived by this procedure includes only the shape noise and hence does not include cosmic shear from the large-scale structure (see also Appendix 1).

We mask the boundary of the survey region as follows. We first derive the smoothed number density map by first deriving the pixelized number density maps and then smoothing it by a Gaussian kernel with a standard deviation of $8'$. The average number density is derived from the smoothed map with 3σ clipping. We mask pixels that have values less than 0.5 times the average number density. We also mask pixels with values of the sigma map more than 1.5 times higher than the average value.

From the map of the signal-to-noise ratio ν , we select peaks with $\nu \geq 4.7$, which is the threshold adopted also in Miyazaki et al. (2018a). To avoid double counting of clusters, we discard any peaks that have other peaks with higher ν within $4'$ from the peaks. For mass maps with the truncated isothermal filter (TI05 and TI20), we create mass maps with four different values of z_{min} as shown in Table 1. We create a list of peaks for each value of z_{min} , and combine four lists of peaks with matching radius of $4'$. For a peak that is detected in multiple mass maps from different source galaxy selections, we adopt the highest value of ν among the mass maps as the signal-to-noise ratio of that peak.

4 Results

4.1 Shear-selected cluster catalogs and redshift assignments

We construct shear-selected cluster catalogs from peaks with $\nu \geq 4.7$ in mass maps covering $\sim 510 \text{ deg}^2$ following the procedure described in subsection 3.4. The catalogs are constructed for the three set-ups (TG15, TI05, and TI20) summarized in Table 1. The catalogs contain 187, 418,

and 200 clusters for TG15, TI05, and TI20, respectively. Compared with the TG15 set-up adopted in Miyazaki et al. (2018a), we find roughly twice the number of shear-selected clusters for TI05, because the shape of the kernel function for TI05 follows the expected tangential shear profile more closely than for TG15 and therefore is more optimal. The small number of shear-selected clusters for TI20, on the other hand, is due to the removal of the large central region ($< 2'$) where a significant tangential shear signal is observed for many clusters. Figure 2 shows the spatial distribution of these clusters from peaks in mass maps. We note that, even though the numbers of shear-selected clusters are similar between TG15 and TI20, roughly half of the clusters are detected both in TG15 and TI20, partly because most of the clusters have signal-to-noise ratios near the threshold (see below).

To check whether they are indeed associated with concentrations of red galaxies and to assign redshifts to these clusters, we cross match the shear-selected cluster catalogs with four optically-selected cluster catalogs, HSC CAMIRA, SDSS redMaPPer, SDSS WHL15, and SDSS CODEX (see subsection 2.2 for concise descriptions of these catalogs). We regard any optically-selected clusters that are located within the physical transverse distance of $1h^{-1}\text{Mpc}$ computed at the cluster redshifts from each shear-selected cluster as matched clusters. It is possible that multiple optically-selected clusters are matched with a single shear-selected cluster, and in that case we regard an optically-selected cluster that is located closest to the shear-selected cluster, whose location refers to a peak position in a mass map, in terms of the physical transverse distance as a primary match and assign the photometric redshift of the primarily matched cluster to the shear-selected cluster.

The result of matching is summarized in Table 2. For TG15 and TI20, $\sim 97\%$ of shear-selected clusters

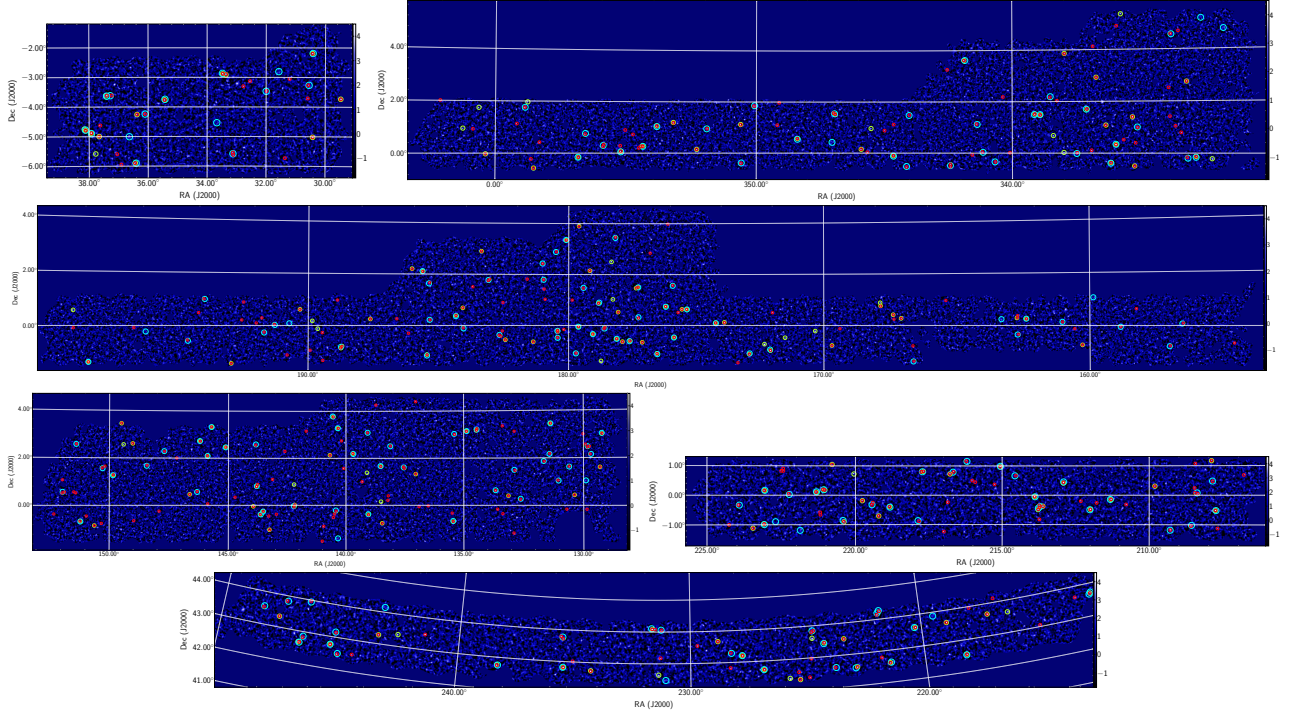


Fig. 2. The spatial distribution of identified shear-selected clusters i.e., peaks in mass maps, in six disjoint patches. Middle green, small red, large cyan circles show clusters by TG15, TI05, and TI20 set-ups (see Table 1), respectively. They are overlaid in mass maps created by the Gaussian filter without the truncation ($\theta_{\text{out}} \rightarrow \infty$ in equation 6) with $\theta_0 = 2'$.

Table 2. Summary of shear-selected cluster samples and matching with optically-selected cluster catalogs. The last column shows the number of shear-selected clusters that are matched with any of optically-selected cluster catalogs and thus with redshift assignments.

Name	Num. of clusters	CAMIRA match*	redMaPPer match*	WHL15 match*	CODEX match*	Any match
TG15	187	163 (21)	135 (7)	177 (50)	59 (6)	182
TI05	418	353 (51)	271 (11)	364 (104)	124 (6)	392
TI20	200	173 (33)	138 (10)	184 (69)	79 (3)	193

* The number in parentheses indicates shear-selected clusters that are matched with multiple optically-selected clusters.

have counterparts in optically-selected cluster catalogs and hence have redshift assignments. The fraction slightly decreases to $\sim 94\%$ for TI05. For comparison, we generate a random catalog of shear-selected clusters by randomly drawing points in unmasked regions of mass maps with the number density of 5 deg^{-2} , and apply the same method for matching shear-selected clusters with the optically-selected clusters to find that $\sim 33\%$ of the random shear-selected clusters are matched with any of optically-selected clusters. Since this fraction represents the chance probability of matching with the optically-selected clusters, we can argue that the true fraction of unmatched shear-selected clusters may be as high as $3 \times 3/2 \sim 5\%$ for TG15 and TI20, and $6 \times 3/2 \sim 9\%$ for TI05. Taking also the incompleteness of our optically-selected cluster samples used for matching (e.g., no cluster at $z < 0.05$) into consideration,

we can argue that the purity of our shear-selected cluster catalogs is higher than 95% for TG15 and TI20 and more than 91% for TI05. The catalogs of the shear-selected clusters for TG15, TI05, and TI20 set-ups including the results of cross matching are shown in Supplementary Tables 1, 2, and 3.

We show distributions of the signal-to-noise ratio ν and the redshift z_{cl} of shear-selected clusters for all the three set-ups in Figures 3 and 4, respectively. Number counts rapidly decrease with increasing ν and the redshift distributions are peaked at $z_{\text{cl}} \sim 0.2 - 0.3$, both of which are consistent with theoretical predictions (see e.g., Miyazaki et al. 2018a).

While weak lensing mass maps are constructed from E-mode shear, B-mode mass maps generated from B-mode shear provide an important means of checking the validity

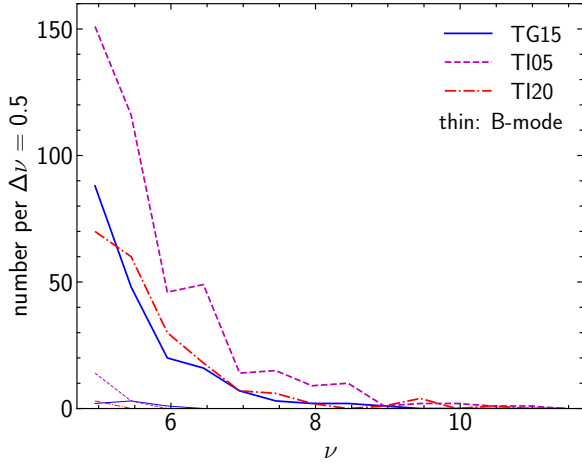


Fig. 3. Distributions of the signal-to-noise ratio ν . Solid, dashed, and dash-dotted lines show distributions for the TG15, TI05, TI20 set-ups summarized in Table 1, respectively. Thin lines indicate distributions of the signal-to-noise ratio ν from B-mode mass map peaks.

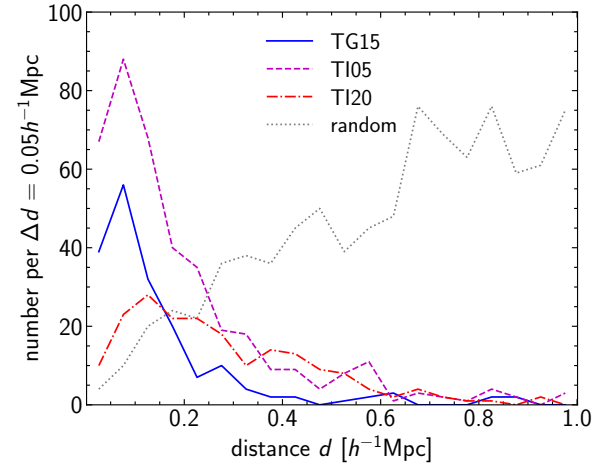


Fig. 5. Similar to Figure 3, but distributions of the physical transverse distance d between the shear-selected cluster and the primarily matched optically-selected cluster are shown. The distribution of d for the case using the random catalog is also shown by the dotted line for reference.

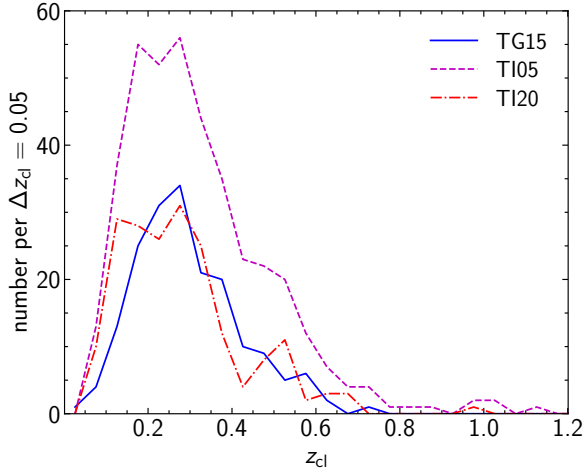


Fig. 4. Similar to Figure 3, but distributions of cluster redshift z_{cl} are shown.

of the analysis (e.g., Utsumi et al. 2014). As a sanity check, we select mass map peaks from B-mode mass maps adopting the same signal-to-noise ratio threshold of $\nu \geq 4.7$. The distribution of B-mode mass map peaks are also shown in Figures 3. In total there are 6, 17, and 3 B-mode mass map peaks with $\nu \geq 4.7$ for TG15, TI05, and TI20, respectively. We find that the numbers of B-mode mass map peaks are sufficiently small, $\lesssim 4\%$, compared with those of E-mode mass map peaks, which support the high purity of our shear-selected cluster catalogs as estimated above.

In Figure 5, we show distributions of the physical transverse distance between the shear-selected cluster and the primarily matched optically-selected cluster. We find that in most cases the distance is small, $\lesssim 0.3 h^{-1} \text{Mpc}$. The mean distance is higher for TI20 than in the other set-ups, which

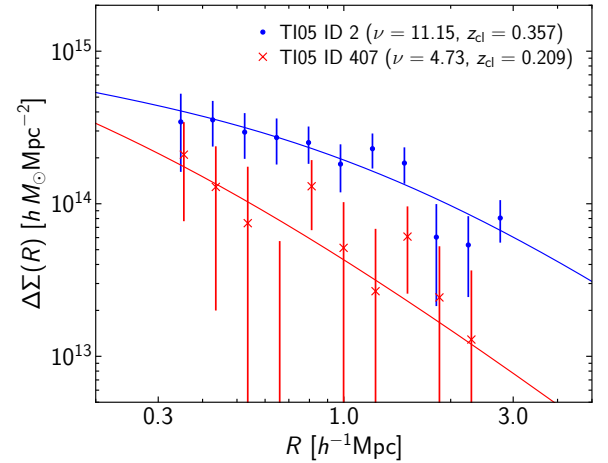


Fig. 6. Examples of tangential shear profiles and fitting them with an NFW profile. We show examples for high and low signal-to-noise ratio ν from the TI05 catalog. Symbols with errors show observed tangential shear profiles, and lines indicate best-fit NFW profiles. Errors include only the shape noise.

can be understood by the conservative choice of $Q(\theta)$ to remove the small-scale information (see Figure 1), which naturally leads to the degraded angular resolution of the resulting mass maps. For comparison, we also plot the distribution in the case of using the random catalog mentioned above. Since the spatial distribution of the random catalog is not correlated with any of optically selected clusters, the resulting distribution indicates that expected for matching by chance. We find that the distribution for the random catalog differs considerably from those for shear-selected clusters, supporting the high purity of our shear-selected cluster catalogs.

4.2 Weak lensing mass measurements

Following Miyazaki et al. (2018a), we derive weak lensing masses of all the shear-selected clusters with redshift assignments by fitting their differential surface density profiles. We use the P-cut method (Oguri 2014; Medezinski et al. 2018) to securely select background galaxies for each shear-selected cluster, adopting $z_{\min} = z_{\text{cl}} + 0.2$ and $P_{\text{th}} = 0.98$ in equation (1). We derive the differential surface density profile $\Delta\Sigma(R)$ by fully taking account of the PDF of the photometric redshift of each galaxy (see e.g., Medezinski et al. 2018, for a specific procedure), again adopting the `dmnz` photometric redshift measurements. For TG15, we derive differential surface density profiles in the range $R = [0.3, 7]h^{-1}\text{Mpc}$ with a spacing of $\Delta\log R = 0.09$. The outer radius is chosen to be same as that used in Miyazaki et al. (2018a) and Chen et al. (2020) so that the mass bias derived in Chen et al. (2020) can be applied. We adopt a slightly larger inner boundary of $R = 0.3h^{-1}\text{Mpc}$ to mitigate the dilution effect by cluster member galaxies (Medezinski et al. 2018). For TI05 and TI20, we adopt a more conservative radius range of $R = [0.3, 3]h^{-1}\text{Mpc}$. In all cases, we consider the shape noise and ignore the cosmic shear error, again to follow the set-up assumed in Chen et al. (2020).

The differential surface density profiles are fitted with an NFW profile (Navarro et al. 1997), which describes differential surface density profiles of clusters in numerical simulations reasonably well out to ~ 10 times the virial radius (Oguri & Hamana 2011). We parameterize the NFW profile by M_{500c} and c_{500c} , which describe the mass and concentration parameter for the critical overdensity of 500. We restrict the range of the concentration parameter to $0.5 < c_{500c} < 10$ and derive both M_{500c} and c_{500c} from fitting to the observed differential surface density profile of each cluster. We show some examples of our tangential shear profile fitting in Figure 6.

The derived weak lensing masses for the TG15, TI05, and TI20 catalogs as a function of the cluster redshift are shown in Figure 7. The fitting results are also given in Supplementary Tables 1, 2, and 3. The increasing trend of weak lensing masses with increasing cluster redshift is theoretically expected for shear-selected clusters (see e.g., Miyazaki et al. 2018a). The massive ($M_{500c} \sim 10^{15}h^{-1}M_{\odot}$) cluster at $z_{\text{cl}} \sim 0.18$ is the well-known cluster Abell 1689 that has one of the largest Einstein radii known (e.g., Oguri & Blandford 2009). Our weak lensing mass estimation of Abell 1689 is consistent with more careful lensing mass estimates in the literature (e.g., Umetsu & Broadhurst 2008; Umetsu et al. 2015).

In Figure 7, we indicate clusters that are matched

with the CODEX catalog. Only less than half of shear-selected clusters are matched with CODEX clusters (see also Table 1), which is partly due to the shallow RASS X-ray data that is used to construct the CODEX catalog (Finoguenov et al. 2020). As a sanity check, we compare our weak lensing masses with X-ray luminosities provided by the CODEX catalog. Figure 8 shows the comparison of weak lensing masses with X-ray luminosities for the TI05 catalog. As expected, we find a good correlation between the masses and the X-ray luminosities. We note that deriving the underlying scaling relation requires the correction of selection biases of both the weak lensing selections in HSC-SSP and the X-ray selection in RASS. We plan to study X-ray properties of these shear-selected clusters in more detail using the eROSITA Final Equatorial Depth Survey data that are much deeper than the RASS X-ray data, which will be reported in a separate paper (Ramos-Ceja et al., in prep.).

4.3 Effects of cluster member galaxies

Cluster member galaxies affect weak lensing measurements mainly in two ways. One is the enhancement of the number density of source galaxies due to the contribution of cluster member galaxies, which dilutes weak lensing signals. The other is the diminishment of the number density of source galaxies due to the obscuration of small galaxies by cluster member galaxies. The former effect can be mitigated by using only source galaxies located behind clusters for weak lensing measurements. Since these effects are more pronounced near centers of clusters, choosing the kernel function $Q(\theta)$ that has a smaller contribution from small θ can also mitigate the effects of cluster member galaxies. Here we check number density profiles of our source galaxy samples around massive clusters to check how our weak lensing mass maps are affected by cluster member galaxies.

To reduce the statistical noise, we derive stacked number density profiles of source galaxies for samples of massive clusters. Purely optically-selected clusters are not ideal for this purpose, because some of optically-selected clusters exhibit large off-centering up to ~ 1 Mpc, which needs to be taken into account when interpreting observed stacked number density profiles. Thus we adopt the CODEX cluster catalog and stack number density profiles around X-ray centroids of CODEX clusters, because X-ray emission peaks are expected to be close to halo centers (e.g., Zhang et al. 2019).

Figure 9 shows stacked number density profiles for three CODEX cluster samples with different cluster redshifts. We also apply the richness cut for each cluster sample in

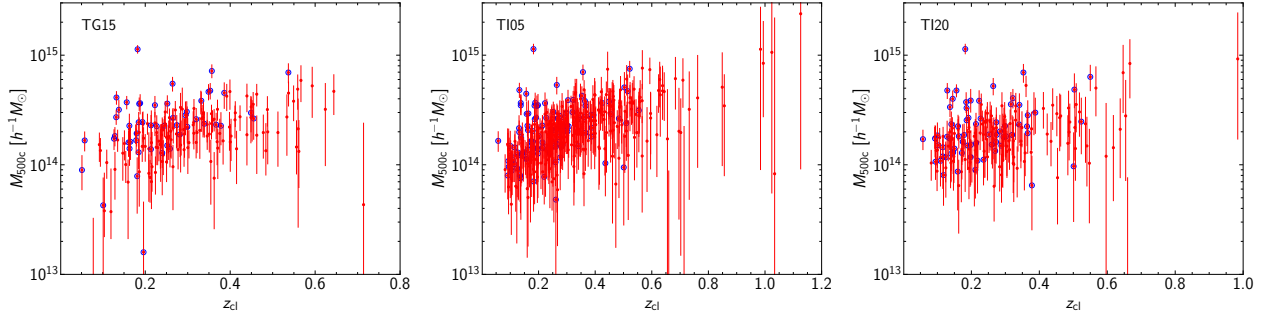


Fig. 7. Weak lensing masses and redshifts of shear-selected clusters in the TG15 (*left*), TI05 (*middle*), and TI20 (*right*) catalogs. Red filled circles with 1σ errorbars show M_{500c} derived from differential surface density profile fitting. Blue open circles indicate clusters that are matched with the CODEX catalog.

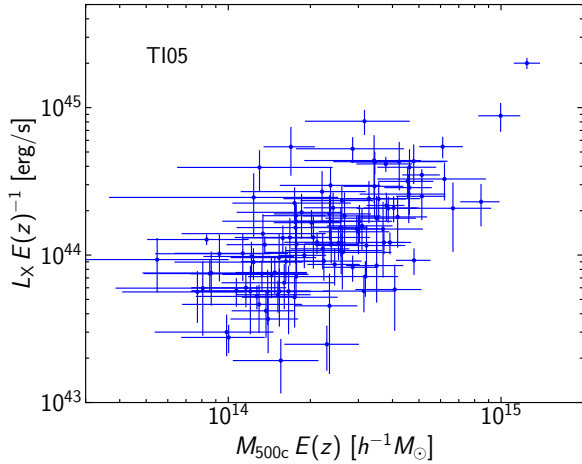


Fig. 8. Weak lensing masses of shear-selected clusters in the TI05 catalog are compared with X-ray luminosities of CODEX clusters that are matched with the shear-selected clusters, with the correction of the dimensionless Hubble parameter $E(z)$. The X-ray luminosities are measured in the rest-frame 0.1 – 2.4 keV (Finoguenov et al. 2020).

order to select clusters with many cluster member galaxies, where the richness λ for CODEX clusters is measured using the redMaPPer algorithm (Rykoff et al. 2014). The richness threshold is determined so that a sufficient ($\gtrsim 50$) number of clusters are included in each of the cluster subsamples. We show stacked number density profiles normalized by those computed with random source galaxy catalogs in order to highlight effects of cluster member galaxies. We find a clear signature of the enhancement of number density profiles without any background galaxy selection. On the other hand, when source galaxies behind clusters are selected, we see decrements toward cluster centers due to the obscuration by cluster member galaxies (or magnification effects, see e.g., Chiu et al. 2020). We find that decrements are negligibly small at $\theta > 2'$, suggesting that the TI20 catalog is little affected by cluster member galaxy obscurations. In contrast, the TG15 and TI05 catalogs are more or less affected by cluster member galaxies

in the sense that the observed signal-to-noise ratios may be affected by the dilution or obscuration effect due to cluster member galaxies. Since cluster member galaxies do not contribute to the signal, the dilution effect enhances the noise and reduce the signal-to-noise ratio. The obscuration affects both the signal and noise in a complicated manner. These effects may be needed to be taken into account when deriving an accurate selection function of shear-selected clusters in the TG15 and TI05 catalogs.

5 Conclusion

We have constructed shear-selected cluster catalogs by selecting peaks in weak lensing aperture mass maps covering $\sim 510 \text{ deg}^2$ reconstructed by the HSC-SSP S19A shape catalog. Aperture mass maps are constructed using the truncated Gaussian filter (TG15) as well as the truncated isothermal filter with the inner boundary of $0.5'$ (TI05) and $2'$ (TI20). For TI05 and TI20, we employ multiple source galaxy subsamples for which galaxies below redshift z_{\min} are removed to improve the efficiency. With the signal-to-noise ratio threshold of 4.7, our shear-selected cluster catalogs contain 187, 418, and 200 clusters for the TG15, TI05, and TI20 set-ups, respectively. Cross matching with optically-selected cluster catalogs suggests that the purity of the catalogs is high, more than 95% for TG15 and TI20 and more than 91% for TI05.

These catalogs represent by far the largest catalogs of shear-selected clusters to date with such high signal-to-noise threshold, and will be useful for detailed studies of cluster astrophysics and cosmology. In this paper, we have demonstrated how the shape of the kernel function for constructing the aperture mass map can be optimized adopting a flexible functional form of the filter function proposed by Schneider (1996). In particular, we have found that it is possible to choose the filter function such that it is almost free from effects of cluster member galaxies yet can select a sufficiently large number of clusters.

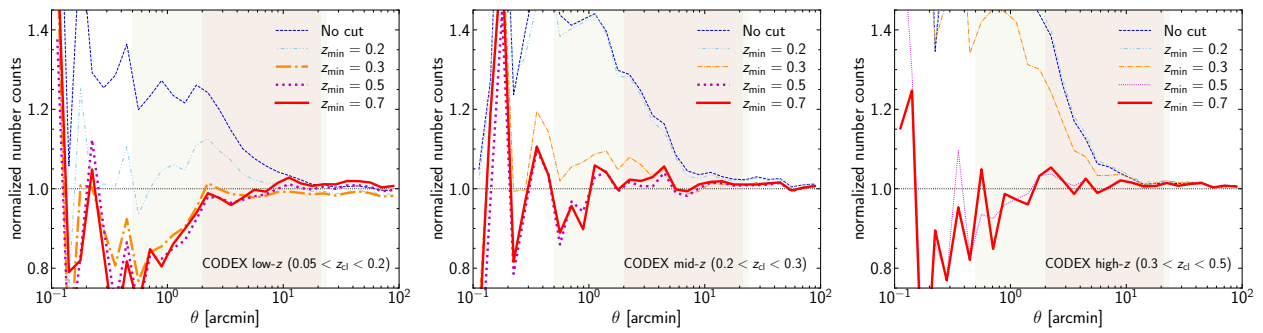


Fig. 9. Stacked number density profiles of source galaxies around CODEX clusters. Here we show number density profiles relative to those from random source catalogs with their total numbers matched to total numbers of source galaxy samples such that the normalized number density profile should be unity if there is no effect of cluster member galaxies. Different lines show results for different source galaxy samples summarized in Table 1. From left to right panels, stacking is conducted around low redshift clusters at $0.05 < z_{cl} < 0.2$ with richness $\lambda > 25$, intermediate redshift clusters at $0.2 < z_{cl} < 0.3$ with $\lambda > 30$, and high redshift clusters at $0.3 < z_{cl} < 0.4$ with $\lambda > 40$. Results for background source galaxy samples satisfying $z_{min} \geq z_{cl} + 0.1$ for all the clusters are highlighted by thick lines. The narrow and wide shaded regions indicate the non-zero ranges of the kernel function $Q(\theta)$ for T120 and T105, respectively (see also Figure 1).

Such a clean shear-selected cluster sample will be useful for obtaining accurate and robust constraints on cosmological parameters from the cluster abundance, in contrast to optically-selected clusters for which constraining power appears to be limited by various systematic effects (Abbott et al. 2020). We will explore cosmological constraints with shear-selected clusters in a forthcoming paper.

Acknowledgments

We thank T. Hamana and K. Umetsu for useful discussions and comments. This work was supported in part by the World Premier International Research Center Initiative (WPI Initiative), MEXT, Japan, and JSPS KAKENHI Grant Nos. JP18K03693, JP20H00181, JP20H05856. This work was supported in part by Japan Science and Technology Agency (JST) CREST JPMHCR1414, and by JST AIP Acceleration Research Grant No. JP20317829, Japan.

The Hyper Suprime-Cam (HSC) collaboration includes the astronomical communities of Japan and Taiwan, and Princeton University. The HSC instrumentation and software were developed by the National Astronomical Observatory of Japan (NAOJ), the Kavli Institute for the Physics and Mathematics of the Universe (Kavli IPMU), the University of Tokyo, the High Energy Accelerator Research Organization (KEK), the Academia Sinica Institute for Astronomy and Astrophysics in Taiwan (ASIAA), and Princeton University. Funding was contributed by the FIRST program from the Japanese Cabinet Office, the Ministry of Education, Culture, Sports, Science and Technology (MEXT), the Japan Society for the Promotion of Science (JSPS), Japan Science and Technology Agency (JST), the Toray Science Foundation, NAOJ, Kavli IPMU, KEK, ASIAA, and Princeton University.

This paper makes use of software developed for the Large Synoptic Survey Telescope. We thank the LSST Project for making their code available as free software at <http://dm.lsst.org>

This paper is based on data collected at the Subaru Telescope

and retrieved from the HSC data archive system, which is operated by Subaru Telescope and Astronomy Data Center (ADC) at NAOJ. Data analysis was in part carried out with the cooperation of Center for Computational Astrophysics (CfCA), NAOJ.

The Pan-STARRS1 Surveys (PS1) and the PS1 public science archive have been made possible through contributions by the Institute for Astronomy, the University of Hawaii, the Pan-STARRS Project Office, the Max Planck Society and its participating institutes, the Max Planck Institute for Astronomy, Heidelberg, and the Max Planck Institute for Extraterrestrial Physics, Garching, The Johns Hopkins University, Durham University, the University of Edinburgh, the Queen's University Belfast, the Harvard-Smithsonian Center for Astrophysics, the Las Cumbres Observatory Global Telescope Network Incorporated, the National Central University of Taiwan, the Space Telescope Science Institute, the National Aeronautics and Space Administration under grant No. NNX08AR22G issued through the Planetary Science Division of the NASA Science Mission Directorate, the National Science Foundation grant No. AST-1238877, the University of Maryland, Eotvos Lorand University (ELTE), the Los Alamos National Laboratory, and the Gordon and Betty Moore Foundation.

References

- Abbott, T. M. C., Aguena, M., Alarcon, A., et al. 2020, Phys. Rev. D, 102, 023509
- Aihara, H., Allende Prieto, C., An, D., et al. 2011, ApJS, 193, 29
- Aihara, H., Armstrong, R., Bickerton, S., et al. 2018a, PASJ, 70, S8
- Aihara, H., Arimoto, N., Armstrong, R., et al. 2018b, PASJ, 70, S4
- Aihara, H., AlSayyad, Y., Ando, M., et al. 2019, PASJ, 71, 114
- Allen, S. W., Evrard, A. E., & Mantz, A. B. 2011, ARA&A, 49, 409
- Bartelmann, M. 1996, A&A, 313, 697

- Chen, K.-F., Oguri, M., Lin, Y.-T., & Miyazaki, S. 2020, *ApJ*, 891, 139
- Chiu, I. N., Umetsu, K., Murata, R., Medezinski, E., & Oguri, M. 2020, *MNRAS*, 495, 428
- Diemer, B., & Joyce, M. 2019, *ApJ*, 871, 168
- Diemer, B., & Kravtsov, A. V. 2015, *ApJ*, 799, 108
- Dietrich, J. P., & Hartlap, J. 2010, *MNRAS*, 402, 1049
- Ebeling, H., Edge, A. C., & Henry, J. P. 2001, *ApJ*, 553, 668
- Fan, Z., Shan, H., & Liu, J. 2010, *ApJ*, 719, 1408
- Finoguenov, A., Rykoff, E., Clerc, N., et al. 2020, *A&A*, 638, A114
- Gavazzi, R., & Soucail, G. 2007, *A&A*, 462, 459
- Giles, P. A., Maughan, B. J., Hamana, T., et al. 2015, *MNRAS*, 447, 3044
- Gladders, M. D., & Yee, H. K. C. 2000, *AJ*, 120, 2148
- Hamana, T., Oguri, M., Shirasaki, M., & Sato, M. 2012, *MNRAS*, 425, 2287
- Hamana, T., Sakurai, J., Koike, M., & Miller, L. 2015, *PASJ*, 67, 34
- Hamana, T., Shirasaki, M., & Lin, Y.-T. 2020, *PASJ*, 72, 78
- Hamana, T., Takada, M., & Yoshida, N. 2004, *MNRAS*, 350, 893
- Hennawi, J. F., & Spergel, D. N. 2005, *ApJ*, 624, 59
- Hetterscheidt, M., Erben, T., Schneider, P., et al. 2005, *A&A*, 442, 43
- Heymans, C., Van Waerbeke, L., Miller, L., et al. 2012, *MNRAS*, 427, 146
- Hilton, M., Sifón, C., Naess, S., et al. 2021, *ApJS*, 253, 3
- Hirata, C., & Seljak, U. 2003, *MNRAS*, 343, 459
- Jain, B., & Van Waerbeke, L. 2000, *ApJL*, 530, L1
- Kacprzak, T., Kirk, D., Friedrich, O., et al. 2016, *MNRAS*, 463, 3653
- Kaiser, N., & Squires, G. 1993, *ApJ*, 404, 441
- Kravtsov, A. V., & Borgani, S. 2012, *ARA&A*, 50, 353
- Lin, C.-A., Kilbinger, M., & Pires, S. 2016, *A&A*, 593, A88
- Liu, J., Petri, A., Haiman, Z., et al. 2015a, *Phys. Rev. D*, 91, 063507
- Liu, X., Pan, C., Li, R., et al. 2015b, *MNRAS*, 450, 2888
- Mandelbaum, R., Miyatake, H., Hamana, T., et al. 2018a, *PASJ*, 70, S25
- Mandelbaum, R., Lanusse, F., Leauthaud, A., et al. 2018b, *MNRAS*, 481, 3170
- Marian, L., Smith, R. E., Hilbert, S., & Schneider, P. 2012, *MNRAS*, 423, 1711
- Maturi, M., Angrick, C., Pace, F., & Bartelmann, M. 2010, *A&A*, 519, A23
- Maturi, M., Meneghetti, M., Bartelmann, M., Dolag, K., & Moscardini, L. 2005, *A&A*, 442, 851
- Medezinski, E., Oguri, M., Nishizawa, A. J., et al. 2018, *PASJ*, 70, 30
- Miyazaki, S., Hamana, T., Ellis, R. S., et al. 2007, *ApJ*, 669, 714
- Miyazaki, S., Hamana, T., Shimasaku, K., et al. 2002, *ApJL*, 580, L97
- Miyazaki, S., Oguri, M., Hamana, T., et al. 2015, *ApJ*, 807, 22
- . 2018a, *PASJ*, 70, S27
- Miyazaki, S., Komiyama, Y., Kawanomoto, S., et al. 2018b, *PASJ*, 70, S1
- Navarro, J. F., Frenk, C. S., & White, S. D. M. 1997, *ApJ*, 490, 493
- Oguri, M. 2014, *MNRAS*, 444, 147
- Oguri, M., & Blandford, R. D. 2009, *MNRAS*, 392, 930
- Oguri, M., & Hamana, T. 2011, *MNRAS*, 414, 1851
- Oguri, M., Lin, Y.-T., Lin, S.-C., et al. 2018a, *PASJ*, 70, S20
- Oguri, M., Miyazaki, S., Hikage, C., et al. 2018b, *PASJ*, 70, S26
- Planck Collaboration, Ade, P. A. R., Aghanim, N., et al. 2016, *A&A*, 594, A27
- Pratt, G. W., Arnaud, M., Biviano, A., et al. 2019, *Space Sci. Rev.*, 215, 25
- Rykoff, E. S., Rozo, E., Busha, M. T., et al. 2014, *ApJ*, 785, 104
- Schirmer, M., Erben, T., Hetterscheidt, M., & Schneider, P. 2007, *A&A*, 462, 875
- Schneider, P. 1996, *MNRAS*, 283, 837
- Shan, H., Kneib, J.-P., Tao, C., et al. 2012, *ApJ*, 748, 56
- Shan, H., Liu, X., Hildebrandt, H., et al. 2018, *MNRAS*, 474, 1116
- Shan, H. Y., Kneib, J.-P., Comparat, J., et al. 2014, *MNRAS*, 442, 2534
- Takahashi, R., Sato, M., Nishimichi, T., Taruya, A., & Oguri, M. 2012, *ApJ*, 761, 152
- Tanaka, M., Coupon, J., Hsieh, B.-C., et al. 2018, *PASJ*, 70, S9
- Umetsu, K. 2020, *A&AR*, 28, 7
- Umetsu, K., & Broadhurst, T. 2008, *ApJ*, 684, 177
- Umetsu, K., Sereno, M., Medezinski, E., et al. 2015, *ApJ*, 806, 207
- Utsumi, Y., Miyazaki, S., Geller, M. J., et al. 2014, *ApJ*, 786, 93
- Voges, W., Aschenbach, B., Boller, T., et al. 1999, *A&A*, 349, 389
- Wen, Z. L., & Han, J. L. 2015, *ApJ*, 807, 178
- Wen, Z. L., Han, J. L., & Liu, F. S. 2012, *ApJS*, 199, 34
- White, M., van Waerbeke, L., & Mackey, J. 2002, *ApJ*, 575, 640
- Wittman, D., Dell’Antonio, I. P., Hughes, J. P., et al. 2006, *ApJ*, 643, 128
- Wittman, D., Tyson, J. A., Margoniner, V. E., Cohen, J. G., & Dell’Antonio, I. P. 2001, *ApJL*, 557, L89
- York, D. G., Adelman, J., Anderson, John E., J., et al. 2000, *AJ*, 120, 1579
- Zhang, Y., Jeltama, T., Hollowood, D. L., et al. 2019, *MNRAS*, 487, 2578

Appendix 1 Optimization of the truncated isothermal filter

We use signal-to-noise ratios of mass map peaks computed assuming the NFW profile (Navarro et al. 1997) to optimize parameters of the truncated isothermal filter presented in subsection 3.3. For each set of parameters, we compute the aperture mass $M_{\text{ap,NFW}}$ at the center of a halo using equation (2) with the convergence assuming an NFW profile (e.g., Bartelmann 1996). For each subsample of source galaxies given in Table 1, we fully take account of the source redshift distribution by adopting the

stacked PDF of the photometric redshift PDFs of all the source galaxies. We also adopt the fitting form of the mass-concentration relation presented by Diemer & Kravtsov (2015) and Diemer & Joyce (2019). The signal-to-noise ratio is then computed as

$$\nu_{\text{NFW}} = \frac{M_{\text{ap,NFW}}}{\sigma_{\text{shape}}}, \quad (\text{A1})$$

where σ_{shape} describes the shape noise of the filtered convergence field that is computed as

$$\sigma_{\text{shape}} = \sigma_e \sqrt{\frac{\pi \int d\theta \theta Q^2(\theta)}{n_{\text{gal}}}}, \quad (\text{A2})$$

with σ_e and n_{gal} being the root-mean-square of the ellipticity and the number density of source galaxies, respectively. In this calculation we simply assume $\sigma_e = 0.4$ and $n_{\text{gal}} = 22 \text{ arcmin}^{-2}$ before any source galaxy selection so that the resulting noise of the mass map roughly coincides with that from the real data. For each source galaxy selection we reduce n_{gal} according to the weighted sum of the number of galaxies after the source galaxy selection.

While it is customary to define a sample of shear-selected clusters by applying a threshold to the signal-to-noise ratio that is defined in a manner similar to equation (A1) where only the shape noise is considered, it is known that the accumulated density fluctuations along the line-of-sight (i.e., cosmic shear) also contribute to the noise.

$$\sigma_{\text{LSS}} = \sqrt{\int \frac{\ell d\ell}{2\pi} |\hat{U}(\ell)|^2 C_\ell}, \quad (\text{A3})$$

where $\hat{U}(\ell)$ is the Fourier counterpart of the filter $U(\theta)$ and the cosmic shear power spectrum C_ℓ is related to the nonlinear matter power spectrum $P_{\text{m}}(k; z)$ as

$$C_\ell = \int d\chi \frac{[W^\kappa(\chi)]^2}{\chi^2} P_{\text{m}}(k = \ell/\chi; z), \quad (\text{A4})$$

$$W^\kappa(\chi) = \int_z^\infty dz_s \frac{4\pi G}{c^2} \frac{(\chi_s - \chi)\chi}{\chi_s(1+z)^2} \bar{\rho}_{\text{m}} p(z_s), \quad (\text{A5})$$

where χ and χ_s are the comoving radial distances corresponding to redshift z and z_s , respectively, and $p(z_s)$ denotes the redshift distribution of source galaxies. We use the revised **halofit** model of Takahashi et al. (2012) to compute $P_{\text{m}}(k; z)$. The signal-to-noise ratio including the large-scale structure noise is simply calculated as

$$\nu_{\text{NFW,wLSS}} = \frac{M_{\text{ap,NFW}}}{\sqrt{\sigma_{\text{shape}}^2 + \sigma_{\text{LSS}}^2}}. \quad (\text{A6})$$

We optimize parameters of the truncated isothermal filter as follows. For each source galaxy selection listed in Table 1, we consider NFW halos located at $z = z_{\text{min}} - 0.1$ with varying halo mass as representative halos detected in mass maps with the source galaxy selection characterized

by z_{min} . For each mass of the NFW halo, we vary ν_1 , ν_2 , and θ_R to search for the optimal set of parameters that maximize $\nu_{\text{NFW,wLSS}}$ given by equation (A6). Since the combination of $\nu_1 \theta_R$ determines the inner boundary of the filter (see subsection 3.3), in this paper we consider two cases, $\nu_1 \theta_R = 0.5$ and $2'$. The former is chosen such that the tangential shear at $\theta \sim 1' - 1.5'$, where the contribution to the signal is large, is included. The latter removes the significant fraction of the inner part of the profile from the calculation, and hence is much less affected by various systematic effects as discussed in subsection 3.3 (see also subsection 4.3). First we vary all the three parameters with the constraint on $\nu_1 \theta_R$ to find that $\nu_{\text{NFW,wLSS}}$ is generally maximized for $\nu_2 \sim 0.3 - 0.4$. We thus fix $\nu_2 = 0.36$ throughout the paper and derive the optimal choice of ν_1 and θ_R , as well as ν_{NFW} and $\nu_{\text{NFW,wLSS}}$, as a function of the halo mass. We adopt values of ν_1 and θ_R for the halo mass that yields $\nu_{\text{NFW}} \sim 5$, roughly corresponding to threshold of constructing shear-selected clusters used in the literature. Parameters determined by this procedure for each $\nu_1 \theta_R$ and the source galaxy selection are presented in Table 1.

Appendix 2 Supporting Information

Supplementary Tables 1, 2, and 3 are available online.